Available online at www.sciencedirect.com
SCIENCE DIRECT®
Acta Materialia 52 (2004) 1859–1869
Acta MATERIALIA
www.actamat-journals.com

Adiabatic shear banding in ultrafine-grained Fe processed by severe plastic deformation

Q. Wei [a,*], L. Kecskes [b], T. Jiao [a], K.T. Hartwig [c], K.T. Ramesh [a], E. Ma [a]

[a] Center for Advanced Metallic and Ceramic Systems (CAMCS), Johns Hopkins University, 223 Latrobe Hall, Baltimore, MD 21218, USA
[b] US Army Research Laboratory, Aberdeen Proving Ground, MD 21005, USA
[c] Department of Mechanical Engineering, Texas A&M University, College Station, TX 77843-3123, USA

Received 27 October 2003; received in revised form 15 December 2003; accepted 17 December 2003

Abstract

We have investigated the plastic deformation behavior of ultrafine-grained (UFG) bulk Fe. The UFG microstructure (grain size ~300 and ~150 nm) was obtained through combined equal channel angular extrusion and low-temperature rolling, and confirmed using transmission electron microscopy. Mechanical properties were measured under both quasi-static (strain rate in the range of 10^{-4}–10^{0} s^{-1}) and dynamic (strain rate up to ~10^{3} s^{-1} using the Kolsky bar technique) compressive loading. Dynamic stress–strain curves of the UFG Fe exhibit significant flow softening, in addition to a significant reduction in the strain rate sensitivity of the flow stress. Consequently, under dynamic loading the plastic flow mode changes from the uniform deformation of conventional coarse-grained Fe to substantial localized deformation in UFG Fe. Both in situ high-speed camera movies and post-loading optical and scanning electron microscopy show the development of adiabatic shear bands, observed for the first time in pure Fe under compressive loading conditions. The morphology of the shear bands and the increased propensity for flow localization due to the ultrafine grain structure are explained using established models for adiabatic shear banding.

Keywords: Shear bands; Severe plastic deformation; Ultrafine microstructure; Mechanical properties; Dynamic behavior; Fe

1. Introduction

The plastic deformation behaviors of nanocrystalline (nc) and ultrafine-grained (UFG) materials have drawn tremendous interest due to the scientific and technological importance of the problem. However, most of the documented experimental and theoretical work has been focused on metals with face centered cubic (fcc) crystalline structures [1–6]. For example, deformation twinning in nc aluminum has been predicted via simulation [2,3] and recently observed using transmission electron microscopy (TEM) [6]. Considering that deformation twinning is absent in conventional Al, this observation demonstrates a striking difference that exists between the plastic deformation mechanisms of a coarse-grained material and its nc counterparts. As for body centered cubic (bcc) metals such as Fe, an interesting observation of localized deformation in the form of shear bands has been reported for consolidated UFG/nc Fe under both dynamic and quasi-static compressive loading [7–11]. TEM reveals that inside the shear band, grains have been substantially elongated, suggesting that the shear banding process involves dislocation activities, and is of non-adiabatic nature. The finding of the enhanced propensity for shear banding is important for the use of nc materials in many applications, such as penetrators, high speed machining, understanding of the workability of nc metals, and so forth [12].

Since impurity incorporation during powder preparation and subsequent compaction may introduce complexity in the microstructure and mechanical behavior of the nc material [13], alternative processing routes to obtaining bulk, contamination free nc metals are needed to verify the new deformation mode observed. This is particularly true for bcc Fe that is known to be susceptible to small amounts of interstitial

* Corresponding author. Tel.: +1-410-516-5162; fax: +1-410-516-4316.
E-mail address: qwei@pegasus.me.jhu.edu (Q. Wei).

1359-6454/$30.00
doi:10.1016/j.actamat.2003.12.025

impurities [14]. So far, contamination, imperfect particle bonding and volume flaws such as porosity have been the major artifacts that adversely influence the properties of nc metals. They are also the origin of controversies in the interpretation of various experimental observations, such as an inverse Hall–Petch relationship [1,13].

Severe plastic deformation (SPD) has been demonstrated to be an effective technique for the production of truly bulk, fully dense and contamination-free metals with sub-micron to nanoscale grain sizes [15–24]. Experiments using techniques such as equal channel angular extrusion (ECAE) [15–24], low-temperature or cryo-rolling [5] have shown that materials properties can be tailored over a wide range by changing processing parameters, such as the geometry of tooling [23], processing temperature [5], specimen feeding orientation [25], etc. For example, SPD-processed Armco Fe has been investigated in terms of microstructural evolution [26–29], micro-hardness change, and quasi-static mechanical properties. This processing route affords us the opportunity to examine the flow localization behavior of Fe when its grain size is refined into the nc and UFG regime. In the present work, we characterize systematically the localized plastic deformation under dynamic compressive loading of UFG Fe. The grain refinement will be produced by SPD, and the samples will be in bulk form without porosity and contamination problems. The propensity for shear localization and the properties of the adiabatic shear bands formed are discussed using phenomenological models.

2. Experimental procedure

Commercial purity Fe was extruded for four passes using route C of ECAE at room temperature. The nominal composition of the starting material is 0.0025%C, 0.009 Si, 0.2 Mn, 0.002 P, 0.001 S, 0.041Al, 0.004 N, 0.0143 O (all in weight percentage) with the balance Fe. The tooling of ECAE is 90°, and the cross-section of the work piece is 25.4 mm × 25.4 mm. This tooling introduces an equivalent strain of 1.15 (von Mises strain) through each pass of processing [25,29]. Route C processing returns material elements to their original shape after an even number of successive extrusions [25]. Therefore, four passes of route C results in an equivalent strain of 4.64 in the work piece. Specimens for mechanical testing were cut from the extruded billets using wire electrical discharge machining (EDM). Following the ASTM standards, the specimens for quasi-static loading have a length to width aspect ratio of $\geqslant 2.0$ (rectangular shape), and the specimens for dynamic loading have a length to width aspect ratio of 0.6:1.0. Quasi-static compressive loading at strain rates in the range of $5 \times 10^{-4} \sim 10^{0}$ s^{-1} was performed using an MTS hydro-servo system. Dynamic compressive loading at strain rates of around 10^{3} s^{-1} was performed using the Kolsky bar (or split Hopkinson bar) technique where the specimen is sandwiched between two elastic bars (called the input and output bars). Strain gages are cemented on the elastic bars to measure: (i) the incident pulse generated by an impacting projectile, (ii) the reflected pulse from the input bar/specimen interface, and (iii) the transmitted pulse through the specimen to the output bar. This technique offers the highest possible strain rates in a uni-axial compression test under uniform deformation conditions. Details of the Kolsky bar technique can be found in [30]. To observe the deformation behavior of the specimens under both quasi-static and dynamic compressive loadings, the side faces of the specimens were polished to a mirror finish. In the dynamic loading case, a DRS Hadland Ultra 8 high-speed camera with the ability to record 10^{8} frames per second was employed to record movies of the dynamic deformation of the specimens. The purpose was to clarify whether and when shear banding is involved and its evolution in the plastic deformation of the material in testing. For comparison, quasi-static and dynamic compressive tests were also performed on the control samples, i.e., the same Fe but in the annealed, coarse-grained condition.

To further refine the grain size of the ECAE processed Fe (hereafter referred to as ECAE Fe), a 10.0-mm thick plate was cut off the ECAE processed billet and cooled in a liquid nitrogen reservoir. This piece was then gradually rolled to a thickness of around 1.8 mm using a laboratory rolling mill, resulting in an additional true strain of ~1.7. Specimens for quasi-static and dynamic compressive testing were then prepared from the rolled piece (hereafter referred to as ECAE+R Fe) using EDM.

Both optical microscopy and scanning electron microscopy (SEM) were used to examine the side surfaces of the specimens after compressive loading.

The microstructures of the ECAE as well as the ECAE+R Fe were investigated using TEM. The TEM specimens were prepared using jet polishing with a solution of 5% perchloric +95% acetic acid at 22 °C. TEM observations were conducted using a Philips EM420 microscope operated at 120 kV.

3. Experimental results

3.1. Microstructure of Fe after SPD

Transmission electron microscopy was performed to obtain detailed information about the microstructure of the SPD processed Fe. Fig. 1 shows the bright field (BF) image (a), selected area diffraction (SAD) (inset in (a)) and central dark field (DF) image (b) of the ECAE Fe.

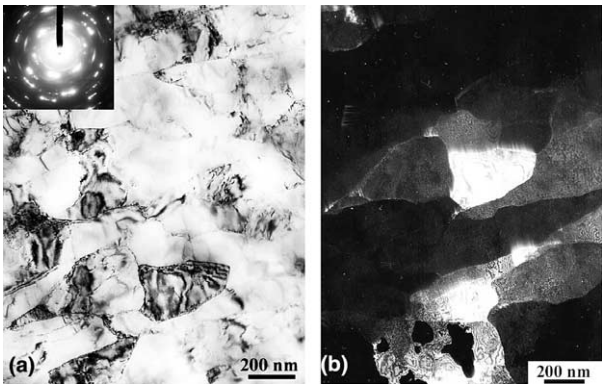

Fig. 1. Bright field TEM micrograph (a), selected area diffraction pattern (inset in (a)) and dark field TEM micrograph (b) of ECAE processed Fe.

The BF and DF images show an average grain size ~300 nm. The shape of the grains is more or less elongated, and many of the grain boundaries are of the low-angle type, typical of the microstructure produced by route C [31–33]. The low-angle grain boundaries are also confirmed by the concentrated diffraction spots and the azimuthal distance between these spots in the SAD pattern. After further low-temperature rolling, the microstructure became ''muddled'', due to the large number of defects stored in the microstructure during additional deformation (Fig. 2(a)). The SAD pattern, obtained using the same size of selection aperture, is shown as an inset in Fig. 2(a). The diffraction rings are still discontinuous, but different from the isolated spots in Fig. 1, suggesting refined grain size. Fig. 2 also displays the corresponding CDF image (Fig. 2(b)). Even though the grain boundaries become less defined, some resolvable grains in these images suggest that the grain size is now approximately 150 nm.

Detailed TEM analysis [26,27] of UFG Fe processed by a different SPD technique showed that large internal stresses might exist in the grains, as indicated by the bending contours in the TEM images. Both the BF and CDF images in Fig. 1 also exhibit intense bending contours, implying large internal stresses induced by the SPD process. Further low-temperature rolling has made this feature even more pronounced, as revealed by the CDF image displayed in Fig. 2(b).

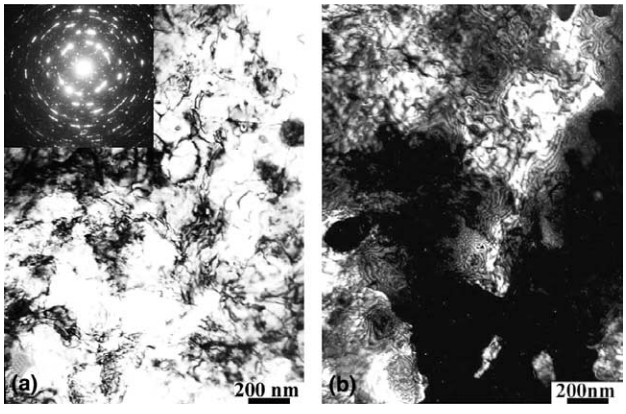

Fig. 2. Bright field TEM image (a), with corresponding SAD pattern (inset in (a)) and dark field TEM image of ECAE+R Fe (b). Note the grain refining by low-temperature rolling, accompanied by increased defect (dislocation) density.

As pointed out in Section 2, ECAE route C was used to process the Fe in this work. The specimen undergoes a rotation of 180° between each extrusion. Extensive studies have been conducted on the effect of various factors of the ECAE process on the microstructure of the worked material, such as the number of passes, temperature, extrusion speed, the size of the work piece, different routes [34–43], etc. It is known that route C tends to produce elongated sub-grain structures with low-angle grain boundaries.

3.2. Mechanical properties

Fig. 3 presents the true stress–strain curves obtained during quasi-static compressive loading of the annealed Fe as well as the ECAE Fe and the ECAE+R Fe. The annealed material exhibits strain hardening typical of bcc Fe, but the yield strength is higher than the ~50 MPa known for high purity Fe [44]. The yield point phenomenon also indicates that some interstitial impurities exist in the material [14]. In contrast, the ECAE Fe behaves in a nearly elastic-perfectly plastic manner at these strain rates (i.e., little strain hardening is observed). Yield strengths above 600 MPa are observed, with the strength increasing slightly with the strain rate.

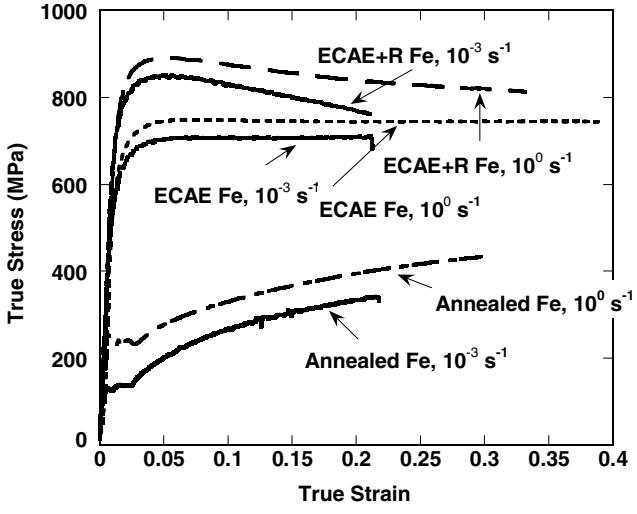

Fig. 3. Quasi-static stress–strain curves under compressive loading for Fe in annealed, ECAE processed, and ECAE+R conditions. Note the significant strain hardening in the annealed Fe which is absent in the SPD processed Fe. Also note the apparently reduced rate dependence in the SPD Fe. The strain rates are given in the figure. See text for the explanation of the slight flow softening in the ECAE+R specimens.

In Fig. 3, it is seen that the yield strength of the ECAE Fe is further increased by about 200 MPa after low-temperature rolling. Apart from the absence of strain hardening, in this case, some slight flow softening is in fact present. This flow softening can be explained as follows. Low-temperature rolling introduces a heavily deformed microstructure, which is retained when the material is brought back to room temperature. Upon loading at room temperature, the relatively fast rate of recovery by means of dislocation annihilation causes softening of the material. Valiev and coworkers [26,27] observed much higher yield strength in the SPD processed Armco Fe (1.2 GPa), but their material had a different level of impurities and the equivalent strain in their case is much higher than in this study. The yield strength reported here for the SPD processed Fe is similar to what has been obtained recently by Han et al. [45], who also observed the exhaustion of strain hardening capacity of Fe after SPD.

It is to be noted that the unloading part of the mechanical testing has not been included in the stress–strain curves, but no sample failure was observed up to the prescribed strain level.

Fig. 4 displays the stress–strain curves under dynamic loading. The strain rate and processing corresponding to each curve are given in the inset. Here, the annealed Fe exhibits significant strain hardening to a strain level of 0.2, and after that the stress–strain curve levels off because of adiabatic heating and subsequent dynamic recovery and recrystallization. Both high-speed camera movie and postmortem optical microscopy show uniform deformation of samples. After ECAE processing,

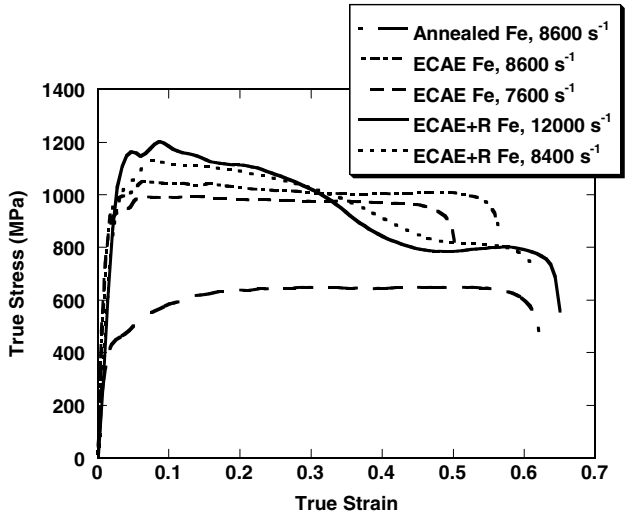

Fig. 4. Dynamic stress–strain curves from Kolsky bar compression tests for Fe in the annealed, ECAE, and ECAE+R conditions. Note the strain hardening in the annealed Fe to a strain of 0.2. The strain hardening is absent in the SPD processed samples. On the contrary, flow softening is observed in these samples, in particular in the ECAE+R state. The strain rates are given in the figure.

the strength is increased by a factor of approximately 2, accompanied by slight flow softening. Comparing the curves in Figs. 3 and 4, the ECAE Fe shows decreased rate sensitivity relative to that of the annealed Fe. This behavior can be explained by recourse to existing constitutive models for bcc metals [8]. Qualitatively, at low temperatures and in single crystal or large grained bcc metals, the yield and flow stresses are large and strongly temperature- and rate-dependent as a direct consequence of the low mobility of the screw dislocations [46,47]. In comparison with this large effective stress, the athermal stress stemming from the dislocation–dislocation interactions is negligible as long as dislocation densities do not reach very large values. But when the grain size is decreased, or with heavily deformed microstructure, another athermal stress from the grain boundaries should be included in the flow or yield stress, and this contribution may become large and eventually prevailing. Since this athermal stress is not rate-sensitive, its increasing contribution renders a bcc metal with small grain size or heavily deformed microstructure less rate dependent as compared to its large-grain counterparts assuming that the Peierls–Nabarro stress is independent of grain size. Fig. 4 also displays the dynamic stress–strain curves for the ECAE+R Fe. The yield strength is further enhanced by ~150 MPa compared to the ECAE state. What is striking is that the ECAE+R Fe exhibits much more pronounced flow softening in comparison with the ECAE Fe. Similar to the ECAE Fe, the rate dependence of the flow stress is reduced compared to the annealed state.

Part of the flow softening in the ECAE Fe and the ECAE+R Fe can be attributed to adiabatic heating, which may become significant when the flow stress level is substantially increased. Under dynamic compression, a yield stress of about 1.0 GPa is observed for ECAE Fe, and above 1.0 GPa for ECAE+R Fe. The adiabatic temperature rise ΔT, developed in such an experiment is

$$\Delta T = \frac{\beta}{\rho C_{\mathrm{p}}} \int_0^{\varepsilon_{\mathrm{f}}} \sigma \, \mathrm{d}\varepsilon, \tag{1}$$

where β is the fraction of plastic work converted into heat (assumed to be 0.9 in this case [48]), ρ is the density (7.9 g/cm^3 for Fe), C_{p} is the specific heat (0.44 J/g K), σ is the flow stress, and ε_{f} is the final strain. For ECAE Fe under dynamic loading, the corresponding temperature rise would be about 100 K when the strain is about 0.4. For the ECAE+R Fe, the temperature rise would be 125 K. These estimated adiabatic temperature rises are for the overall specimen under dynamic compression. A significant temperature sensitivity of the strength is typical of bcc metals [49], including Fe, resulting in the apparent softening observed here. Note again that there is little strain hardening capacity left in the SPD Fe due to the heavily deformed microstructure with high densities of dislocations and small grain sizes [26]. This is

supported by a recent paper [45] that shows further ECAE processing after a certain passes (e.g., four passes) will not increase the hardness of Fe significantly. The exhausted or decreased work-hardening ability in heavily deformed or UFG metals can also be accounted for by invoking the intrinsic size effects in the plasticity of metals [50]. Theoretical consideration of the intrinsic size effect associated with metal plasticity predicts that when the grain size is below a characteristic length scale, work-hardening decreases with decreased grain size. For most metals, this characteristic length scale is a function of forest dislocation density and is around 3.0 micrometers.

Fig. 5 displays the rate dependence of the ECAE Fe, the ECAE+R Fe, along with the annealed Fe. The flow stresses of all the samples at an off-set strain of 0.10 were normalized against the flow stress at 10% strain of the same processed state under a strain-rate of 5×10^{-4} s^{-1} (the lowest strain rate used in this study). A power law in the form of $\sigma/\sigma_0 = (\dot{\varepsilon}/\dot{\varepsilon}_0)^m$ was used to fit the data and the value of the strain rate sensitivity, m, is used as an indicator of the rate dependence of the material. It is seen that the ECAE Fe and the ECAE+R Fe exhibit decreased rate sensitivity compared to the annealed state. The same trend was observed for ECAE Ta in our recent work [24]. The low-temperature rolling process, however, does not introduce further detectable reduction in the rate dependence.

In summary, our tests show that ECAE increases the quasi-static yield strength of Fe by a factor of 4 and dynamic yield strength by a factor of ca. 2. The ECAE Fe exhibits elastic-nearly perfectly plastic behavior and slight flow softening under dynamic loading. Low-temperature rolling increases the yield strength further by about 150 MPa and leads to obvious flow softening under dynamic loading. These changes in properties are expected to influence the deformation mode, as detailed below.

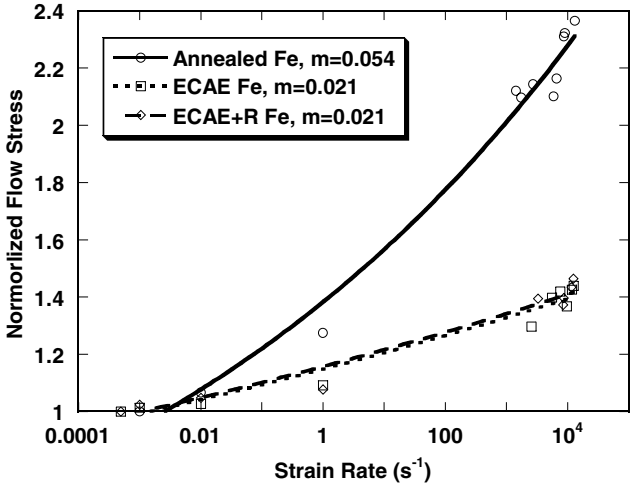

Fig. 5. Rate dependence of different states of Fe. The values of the strain rate sensitivity, m, are given in the figure. Note the substantial reduction in m in the SPD processed Fe in comparison to the annealed state.

3.3. SEM and optical observation of shear bands in SPD processed Fe

Shear banding was observed to be the predominant plastic deformation mechanism under both quasi-static and dynamic compression of consolidated Fe with UFG or nc microstructure, which was processed by mechanical attrition, followed by two-step compaction [7,8]. The grain size that starts to produce pronounced shear localization is around 300 nm. Consolidated Fe with grain size larger than this deforms uniformly under both quasi-static and dynamic loading. A direct comparison with UFG Fe prepared in a "one-step" process [51] without consolidation so that volume flaws and impurity incorporation could be eliminated will be interesting: it is important to confirm that it is the grain size effects that change the propensity for shear banding.

For the annealed as well as the SPD processed Fe in this work, uniform plastic deformation is observed under quasi-static loading for all samples. Annealed Fe also shows uniform deformation under dynamic loading, as expected [8,48]. However, ECAE processed Fe did exhibit signs of localized deformation under dynamic compressive loading. Fig. 6 depicts the concentrated shear in local regions of one of the samples (loading is along the vertical direction). *The specimen was loaded to a true strain level of ~0.55 at a strain rate of ~7000 s^{-1}*. Fig. 6(a) shows the low magnification SEM image of the shear marks (the lines of bright contrast) on the surface of the sample (the sandwiched piece is the specimen). There are two sets of intersecting lines of bright contrast, similar to the consolidated nc and UFG Fe [7,8]. Fig. 6(b) shows the overall view of some of the shear lines. In the figure the whole image has been rotated about 45° clockwise with respect to the loading direction to save space. More detailed structure of the shear lines is revealed in Fig. 6(c), which shows bundles of shear lines with a width of several tens of micrometers. The individual shear lines have a width of several microns. We presume that those shear lines of light contrast are consequence of intense plastic deformation under dynamic loading.

Fig. 7 shows the post-dynamic loading SEM images of the ECAE+R Fe (loading is along the vertical direction). *The specimen was loaded to a true strain level of ~0.6 at a strain rate of around 8000 s^{-1}*. In this case, shear banding is ostensive. The low magnification SEM micrograph in Fig. 7(a) shows two major shear bands. Both the right and the left bands are oriented at an angle of ca. 45° relative to the loading direction. Fig. 7(b) is an enlarged image of the left band in Fig. 7(a), with the

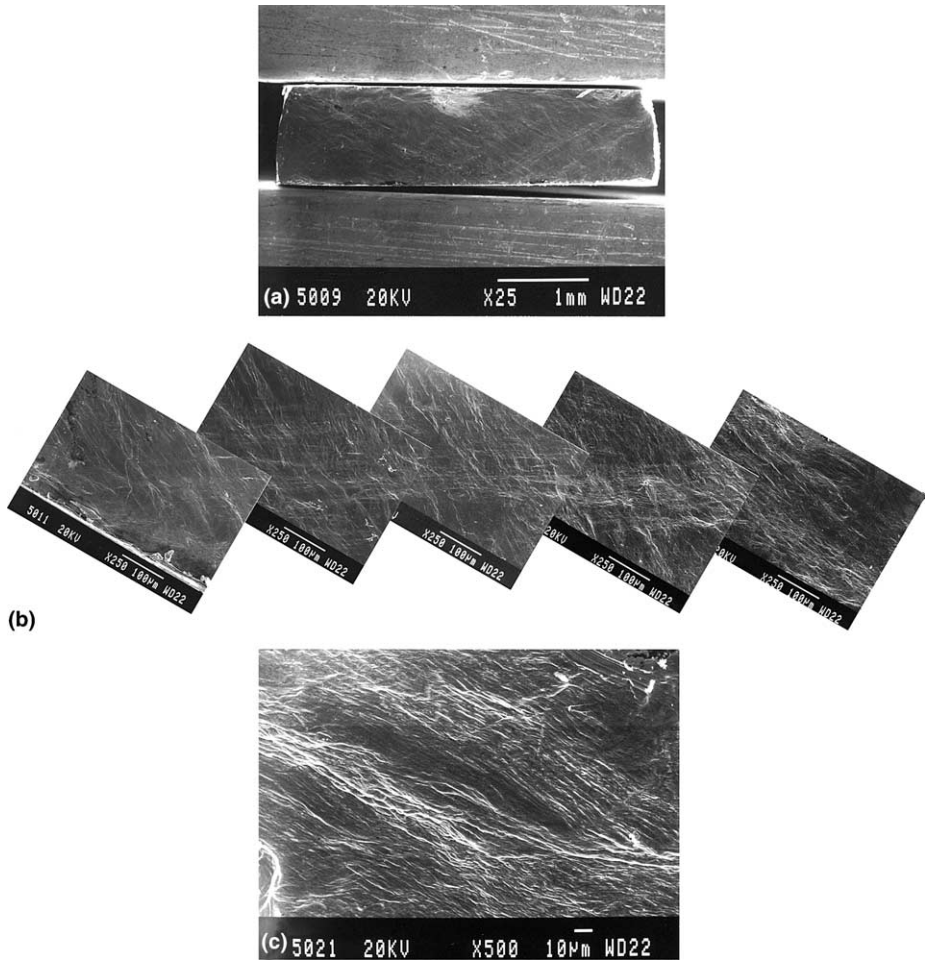

Fig. 6. SEM micrographs of the side face of a dynamically loaded ECAE Fe. (a) Overall surface at a low magnification (loading is along the vertical direction and the sandwiched piece is the specimen); (b) A collage showing the shear band contrast; (c) An enlarged image showing the details of some shear bands. Note that in (b) the specimen has been rotated about 45° clockwise with respect to the loading direction to save space. The specimen was loaded to a true strain of ~0.55 at a strain rate of ~7000 s^{-1}.

details of the areas indicated by arrows given in Fig. 7(c)–(f). (It is to be noted that in Fig. 7(b), the specimen has been rotated ~45° counterclockwise to save space). These images demonstrate that the shear bands have accommodated highly concentrated strains. Shear strain in the range of 5.0–100 is not unusual in the shear band such as reported here [48]. Adiabatic temperature rise in the shear band region larger than 1000 K has been frequently reported in the literature [48]. Bearing in mind that the adiabatic temperature rise computed in the previous section is based on the overall strain to a level of 0.4, we can envisage that the local adiabatic temperature rise within the shear bands must be substantially higher than the average. This explains the microstructure observed in the enlarged images of Fig. 7(c)–(f), corresponding to the areas indicated by the arrows in Fig. 7(b). It is worth noting that the surface was polished to a finish of ca. 1 μm before loading. After loading, the microstructure in the shear band has been significantly elongated, implying large shear strains. This is obvious from Fig. 7(c)–(f). What is more, in Fig. 7(d), a layer of wavy structure within the shear band can be seen, suggesting rotation and twisting of the material therein under dynamic loading. To have a better picture of the shear band, the as-tested sample was polished and then etched using 5% Nital. Fig. 8 shows the etched specimen, where the shear band is clearly revealed with a well-defined width of about 15 μm. *The two white lines are added in order to facilitate the readers to identify the shear band boundaries in the specimen.*

The initiation and evolution of shear localization was also recorded using a high-speed camera. Fig. 9 shows four snap shots of the ECAE+R sample during dynamic compressive loading. The four images correspond to a strain level of 0.0, 0.3, 0.44, and 0.56, respectively. It can be seen from Fig. 9(b) (strain level ~0.3) that shear localization starts around this point. What is interesting in

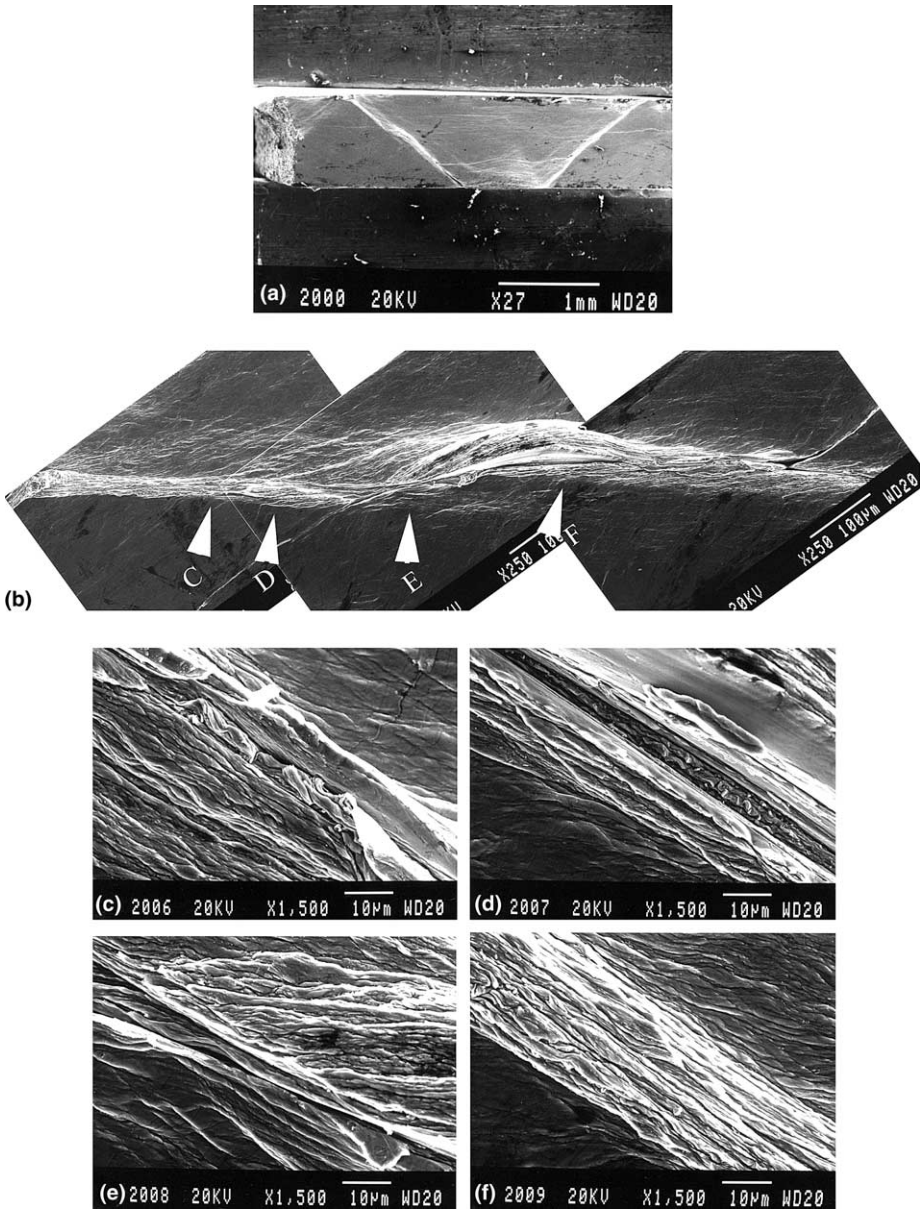

Fig. 7. A low magnification SEM micrograph (a) showing two major shear bands (loading is along the vertical direction, and the sandwiched piece is the specimen). Both the right and the left bands are oriented at an angle of ca. 45° relative to the loading direction. (b) Enlarged image of the left band in (a), with the details of the areas indicated by arrows given in (c)–(f). Note that in (b) the specimen has been rotated about 45° counter-clockwise with respect to the loading direction to save space. The specimen was loaded to a true strain of ~0.6 at a strain rate of ~ 8000 s^{-1}.

this image is the observation that shear localization was initiated at the corner of the specimen. Also recall that this is the strain level where significant load drop is observed in the dynamic stress–strain curve (Fig. 4).

To the best of our knowledge, conventional Fe does *not* exhibit shear localization under conventional compressive Kolsky bar loading. Forced localization may be incurred by special design of the geometry of the specimen that imposes artificial concentrated shear stress during loading. Our finding is, therefore, the first discovery of adiabatic shear localization in Fe. The interpretation of this discovery will be given in the following.

4. Discussion

As has been described in Section 3.3, under dynamic compression localized plastic deformation in the form of adiabatic shear banding (ASB) becomes a dominant plastic deformation mechanism in the UFG Fe processed by SPD, especially for the ECAE processed Fe that was further rolled at low temperature. SEM reveals heavy plastic deformation in the shear band, wherein substantial adiabatic temperature rise should be expected.

Adiabatic shear banding has been reported in Armco Fe under explosive loading [48], the strain rate of which

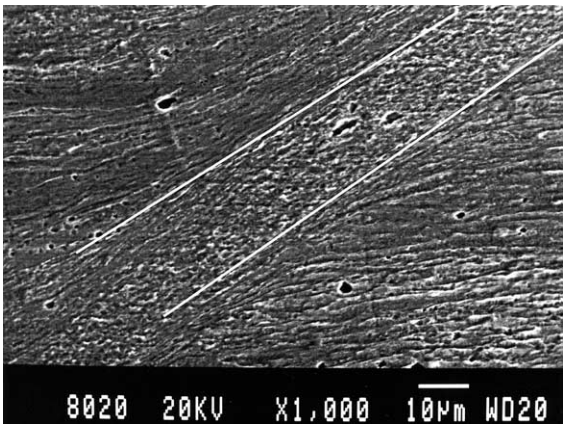

Fig. 8. Post-loading sample was polished and then etched using 5% Nital to reveal the microstructure, where the shear band is clearly seen with a width of about 15 μm. The boundaries of the adiabatic shear band have been marked out by a pair of white lines for the ease of identification.

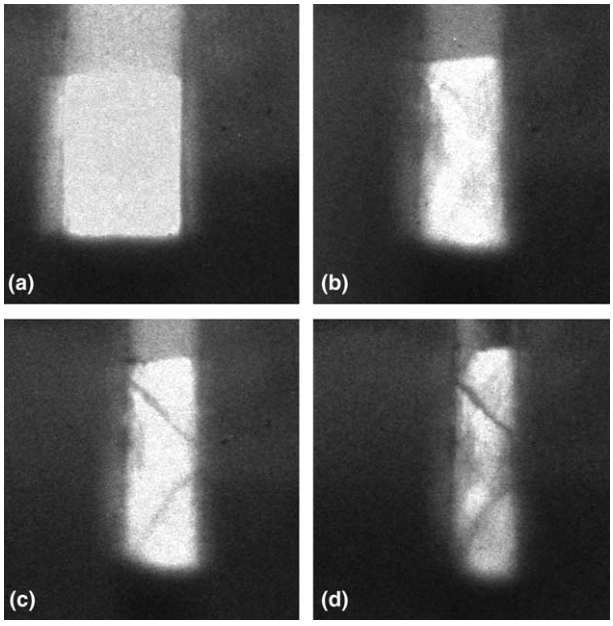

Fig. 9. Snap-shots from the high-speed camera movie of a sample during dynamic loading at the strain rate of $\sim$8000 s^{-1}. The material was ECAE processed followed by low-temperature rolling. The four images correspond to a strain level of 0.0, 0.3, 0.44, and 0.56, respectively. It can be seen from (b) (strain level $\sim$0.3) that shear localization starts around this point.

is much higher than what can be reached by compression Kolsky bar loading. Even at such high strain rates, the critical shear strain required for shear localization to initiate is more than 4.0. In contrast, high-speed camera movies recorded in this work show that, for our SPD processed Fe, the strain level at which ASB sets in is only <0.3.

As pointed out in [48], there are a number of variables that affect the initiation and development of ASB. They can be classified into the following four categories: materials parameters, the stress state, microstructure of the material or external loading conditions. Materials parameters include density, specific heat, thermal conductivity (thermal diffusivity), strain hardening rate, thermal softening rate, and strain rate sensitivity. The factors from the microstructure include size, shape, spacing, orientation, population and distribution of second phase particles, inclusions, precipitates, etc., as well as texture, porosity, imperfections, and thermal stability of the microstructures. External conditions may include disturbances and discontinuities imposed externally, their amplitude, sharpness distributions, and energy.

The beginning of flow localization, or alternatively, flow instability, of a metal under tension is predicted fairly well by the well-known Considére criterion [52]. Under compression, a flow localization parameter, α, can be used to qualitatively discuss the propensity of a metal for flow localization [53,54]. This parameter is a function of two materials properties: the strain-hardening rate, γ, and the strain rate sensitivity, m. A general form of

$$\alpha = (\gamma - 1)/m, \tag{2}$$

describes the relationship among the three parameters, where γ is given by $(1/\sigma)(\partial\sigma/\partial\varepsilon)_{\dot{\varepsilon}}$ into which the thermal effect can be included. Qualitatively, an increased α points to increased propensity for flow localization. Thus, a positive γ and decreased m will favor flow localization. In the case of compressive loading, a positive γ corresponds to flow softening in the true stress–true strain curve.

In Section 3.2, we have shown that m is substantially decreased by SPD and the resulting grain refinement. This decrease in m, together with the flow softening in the SPD Fe, explains qualitatively the flow localization in the form of shear banding under dynamic compressive loading. As mentioned before, the same effect of UFG and nc grain sizes on strain rate hardening, m, and shear banding has been found in several bcc metals, including consolidated nc/UFG Fe and V, and SPD processed Ta [7,8,24,55].

A quantitative description of the susceptibility to ASB by Wright [12,56] gives the following equation:

$$\frac{\chi_{SB}}{a/m} = \min\left\{1, \frac{1}{(n/m) + \sqrt{n/m}}\right\}, \tag{3}$$

where χ_{SB} is the susceptibility to ASB, a is the non-dimensional thermal softening parameter defined by $a = (-\partial\sigma/\partial T)/\rho c$ (σ is the flow stress, T the temperature, ρ the density, and c the specific heat of the material), n the strain hardening exponent, and m the strain rate sensitivity. For a perfectly plastic material (no strain hardening), the susceptibility reduces to

$$\chi_{SB} = \frac{a}{m} = \frac{\lambda\sigma_0}{\rho c m}, \tag{4}$$

where $\lambda = -(1/\hat{\sigma}_0)\partial\sigma/\partial T$ is the thermal softening parameter evaluated under isothermal conditions and σ_0 the yield strength. The susceptibility to ASB of the UFG Fe can thus be estimated to be $\sim 1.7 \times 10^4$ using the following parameters, $\sigma_0 = 1.2$ GPa, $m = 0.02$ from our experimental data (Fig. 4). For the annealed Fe with large grain size, Eq. (3) is to be used with $n = 0.289$ [57]. The resulting χ_{SB} is only ~ 70.

Fig. 8 displays the morphology of the ASB of UFG Fe as revealed by SEM in a polished and etched sample. Boundary layers indicated by the two white lines as predicted by Wright [12] are observed. Within the boundary layers, the microstructure would have a more or less equi-axed morphology due to recrystallization during dynamic loading. The flow lines suggest the canonical structure predicted for ASB [12], where the flow lines bend down through the boundary into the band, and then curve away on the other side forming an anti-symmetric pattern. The disappearance of the flow lines within the shear band implies high temperature rise in the ASB during dynamic loading. This temperature rise might have exceeded the phase transformation temperature for Fe (bcc α-fcc γ transformation temperature for Fe is 912 °C), and subsequent rapid cooling (cooling rate might have exceeded 10^4 s^{-1} [48]) from γ phase would lead to martensitic transformation (the estimated martensitic transformation temperature for pure Fe is around 700 °C [58], with the exact temperature depending critically on the purity of Fe). In low carbon or other steels, this transformation band has higher hardness than the material outside the band [12,48]. On the other hand, dynamic recrystallization would reduce the hardness in the ASB. In our microhardness measurement, no significant difference in hardness was observed between the shear band and material outside. This is an indirect evidence that martensitic transformation might have taken place within the ASB.

Based on perturbation analysis of the uniform solutions to the governing equation of ASB, Bai [59] proposed the following formula for the calculation of half width of the ASB:

$$\delta \approx \left(\frac{kT_*}{\tau_*\dot{\gamma}_*}\right)^{1/2}, \tag{5}$$

where subscript (*) denotes physical quantities within the ASB and k is the thermal conductivity. Numerical and analytical [12,60] results both showed that the stress remains uniform during the evolution of ASB, i.e., it is independent of the spatial coordinates. Strain rate in the center of ASB is usually 3 orders of magnitude higher than the externally imposed strain rate [12,60]. Therefore, the value of δ can be calculated to be ~ 7.0 μm. In Fig. 8, the width of ASB is revealed to be ~ 15 μm, in reasonable agreement with the prediction given by Eq. (5). As pointed out by Wright [12], the bandwidth calculated using (5) has more to do with the thermal thickness of the ASB. Based on asymptotic analysis of the perturbations to the governing equations, Wright derived the following "mechanical length scale" [12,61]:

$$\delta = \left(\frac{1-m}{m}\frac{\lambda\sigma_0 b^m}{k}\right)^{-1/(1-m)} v_0^{-(1+m)/(1-m)}, \tag{6}$$

where b is a normalizing time and v_0 the imposed driving particle velocity ($\dot{\varepsilon} \cdot H$, H the thickness of the sample). This mechanical length refers to the rapid change in velocity across an ASB. Using the parameters in this study, Eq. (6) yields a half width of only 1.0 μm, much smaller than predicted by Eq. (5). One possible explanation of this discrepancy may be related to the fact that the derivation of Eq. (6) is based on the assumption that no phase transformation occurs in the ASB, and the boundary layer is defined by a sharp drop of strain rate. It is a simple matter to verify that the mechanical length scale given by (6) scales inversely with m, the initial strength, and the imposed driving particle velocity. It is possible, however, that the ASB width in Fig. 8 is controlled by the temperature change across the boundary (Eq. (5)), particularly the phase transformation therein.

5. Summary and concluding remarks

1. Fe processed by four ECAE passes of route C exhibit elastic-nearly perfectly plastic behavior under quasi-static compression, and slight flow softening under dynamic compression. The quasi-static yield strength is increased by a factor of 3–4, and the dynamic yield strength by a factor of more than 2, in comparison with coarse-grained Fe.
2. Further rolling at low temperature from the ECAE processed state increases the strength further, and induces pronounced flowing softening under quasi-static and especially dynamic compression.
3. Severe plastic deformation reduces the strain rate sensitivity of Fe by a factor of 2.
4. By eliminating strain hardening, reducing the strain rate sensitivity and increasing the flow strength, SPD and in particular ECAE+R treatment make Fe susceptible to adiabatic shear banding. ASB is observed for the first time in Fe under Kolsky bar compression. The adiabatic shear band has a width consistent with that determined by the thermal processes within the shear band.
5. Our results suggest that conclusion (4) above can be generalized to other UFG bcc metals, regardless of the processing routes such as consolidation of UFG

powders versus SPD. Therefore, it is the refinement of grain size into the UFG regime that enables the localized flow in bcc metals that would otherwise only undergo uniform deformation. This appears to be an effective way to promote shear localization, which is a desirable mode of plastic deformation and failure in such applications as kinetic energy penetrators.

Acknowledgements

The authors thank Dr. T.W. Wright for useful discussions. This work was performed under the auspices of the Center for Advanced Metallic and Ceramic Systems (CAMCS) at the Johns Hopkins University. This research was sponsored by the US Army Research Laboratory (ARMAC-RTP) and was accomplished under the ARMAC-RTP Cooperative Agreement No. DAAD19-01-2-0003. The views and conclusions contained in this document are those of the authors and should not be interpreted as representing the official policies, either expressed or implied, of the US Army Research Laboratory or the US Government. The US Government is authorized to reproduce and distribute reprints for Government purposes not withstanding any copyright notation hereon.

References

[1] Weertman JR, Farkas D, et al. MRS Bull 1999;24:44.
[2] Yamakov Y, Wolf D, Phillpot SR, Mukherjee AK, Gleiter H. Nat Mater 2000;1:45.
[3] Yamakov Y, Wolf D, Phillpot SR, Gleiter H. Acta Mater 2002;50:5005.
[4] Hasnaoui A, Van Swygenhoven H, Derlet PM. Science 2003;300:1550.
[5] Wang Y, Chen M, Zhou F, Ma E. Nature 2002;419:912.
[6] Chen M, Ma E, Hemker K, Sheng H, Wang Y, Cheng X. Science 2003;300:1275.
[7] Wei Q, Jia D, Ma E, Ramesh KT. Appl Phys Lett 2002;81:1240.
[8] Jia D, Ramesh KT, Ma E. Acta Mater 2003;51:3495.
[9] Jia D, Ramesh KT, Ma E. Scripta Mater 2000;42:73.
[10] Malow TR, Koch CC. Acta Mater 1998;46:6459.
[11] Carsley JE, Fisher A, Milligan WW, Aifantis E. Metal Mater Trans A 1998;29:2261.
[12] Wright TW. The physics and mathematics of adiabatic shear bands. Cambridge: Cambridge Press; 2002.
[13] Koch CC, Narayan J. Mater Res Soc Symp Proc 2001;634:B5.1.3.
[14] Conrad H. In: Zackey VF, editor. High-strength materials. New York: Wiley; 1965.
[15] Jia D, Wang YM, Ramesh KT, Ma E, Zhu YT, Valiev RZ. Appl Phys Lett 2001;79:611.
[16] Lowe TC, Valiev RZ, editors. Investigations and applications of severe plastic deformation. Dordrecht: Kluwer Academic Publishers; 2000.
[17] Zhu YT, Langdon TG, Mishra RS, Semiatin SL, Saran MJ, Lowe TC, editors. Ultrafine grained materials II, TMS Annual Meeting and Exhibition; 2002.
[18] Neishi K, Horita Z, Langdon TG. Mater Sci Eng A 2002;325:54.
[19] Shin DH, Kim BC, Kim YS, Park KT. Acta Mater 2000;48:2247.
[20] Park KT, Kim YS, Lee JG, Shin DH. Mater Sci Eng A 2000;293:165.
[21] Kim J, Kim I, Shin DH. Scripta Mater 2001;45:421.
[22] Shin DH, Kim BC, Park KT, Choo TY. Acta Mater 2000;48:3245.
[23] Valiev RZ, Islamgaliev RK, Alexandrov IV. Prog Mater Sci 2000;45:103.
[24] Wei Q, Jiao T, Mathaudhu SN, Ma E, Hartwig KT, Ramesh KT. Mater Sci Eng A 2003;358:266.
[25] Furukawa M, Horita Z, Nemoto M, Langdon TG. J Mater Sci 2001;36:2835.
[26] Valiev RZ, Ivanisenko YV, Rauch EF, Baudelet B. Acta Mater 1996;44:4705.
[27] Islamgaliev RK, Pyshmintsev IY, Khotinov VA, Korznikov AV, Valiev RZ. Phys Met Metall 1998;86:408.
[28] Valiev RZ, Korznikov AV, Mulyukov RR. Mater Sci Eng A 1993;168:141.
[29] Segal VM. Mater Sci Eng A 1995;197:157.
[30] Follansbee PS. In: Davis JR, Refnes S, editors. Metals handbook. The Hopkinson bar, vol. 8. 9th ed. Metals Park, OH: ASM; 1985. p. 198–203.
[31] Langdon TG, Furukawa M, Horita Z, Nemoto M. In: Lowe TC, Valiev RZ, editors. Investigations and applications of severe plastic deformation. Dordrecht: Kluwer Academic Publishers; 2000. p. 149.
[32] Iwahashi Y, Horita Z, Nemoto M, Langdon TG. Acta Mater 1998;46:3317.
[33] Oh-ishi K, Horita Z, Furukawa M, Nemoto M, Langdon TG. Metall Mater Trans A 1998;29:2011.
[34] Nakashima K, Horita Z, Nemoto M, Langdon TG. Acta Mater 1998;46:1589.
[35] Berbon PB, Furukawa M, Horita Z, Nemoto M, Langdon TG. Metall Mater Trans A 1999;30:1989.
[36] Furukawa M, Iwahashi Y, Horita Z, Nemoto M, Langdon TG. Mater Sci Eng A 1998;257:328.
[37] Yamashita A, Yamaguchi D, Horita Z, Langdon TG. Mater Sci Eng A 2000;284:100.
[38] Horita Z, Fujinami T, Langdon TG. Mater Sci Eng A 2001;318:34.
[39] Furukawa M, Horita Z, Nemoto M, Valiev RZ, Langdon TG. Phil Mag A 1998;78:203.
[40] Xu C, Langdon TG. Scripta Mater 2003;48:1.
[41] Yamaguchi D, Horita Z, Nemoto M, Langdon TG. Scripta Mater 1999;41:791.
[42] Semiatin SL, Berbon PB, Langdon TG. Scripta Mater 2001;44:135.
[43] Gibbs MA, Hartwig KT, Cornwell LR, Goforth RE, Payzant EA. Scripta Mater 1998;39:1699.
[44] Matsui H, Moriya S, Takaki S, Kimura H. Trans JIM 1978;19:163.
[45] Han BQ, Lavernia EJ, Mohamed FA. Met Mater Trans A 2003;34:71.
[46] Kubin LP, Devincre B, Tang M. J Comput-Aided Mater Design 1998;5:31.
[47] Duesbery MS, Vitek V. Acta Mater 1998;46:1481.
[48] Bai Y, Dodd B. Adiabatic shear localization. New York: Pergamon Press; 1992.
[49] Christian JW. Metall Trans A 1983;14:1237.
[50] Sevillano JG, Arizcorreta IO, Kubin LP. Mater Sci Eng A 2001;309–310:393.
[51] Koch CC, Morris DG, Lu K, Inoue A. Mater Res Soc Bull 1999;24:54.
[52] Hart EW. Acta Metall 1967;15:351.
[53] Jonas JJ, Holt RA, Coleman CE. Acta Metall 1976;24:911.
[54] Semiatin SL, Jonas JJ. Formability and workability of metals. Metals Park, OH: ASM; 1984.
[55] Wei Q, Jiao T, Ramesh KT, Ma E. Scripta Mater 2004;50:359.

[56] Wright TW. Int J Plasticity 1992;8:583.
[57] Zerilli FJ, Armstrong RW. J Appl Phys 1987;61:1816.
[58] Wei Qiuming, Kang MK. Met Trans A 1991;22:1761.
[59] Dodd B, Bai Y. Mater Sci Tech 1985;1:38.
[60] Wright TW, Walter JW. J Mech Phys Solids 1987;35:701.
[61] Wright TW, Ockendon H. J Mech Phys Solids 1992;40:1217.